



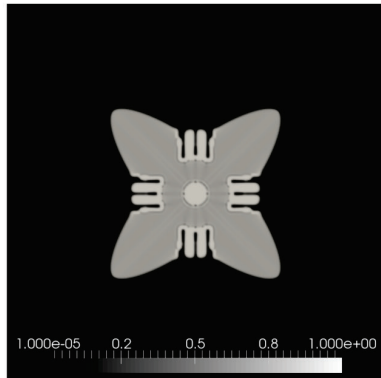
**US Army Corps  
of Engineers®**  
Engineer Research and  
Development Center



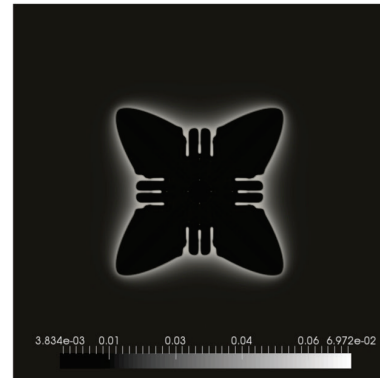
# Phase-Field Simulations of Solidification in Support of Additive Manufacturing Processes

Jeffrey B. Allen, Robert D. Moser, Zachary B. McClelland,  
Jacob A. Kallivayalil, and Arjun Tekalur

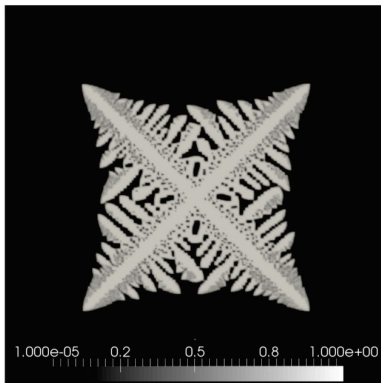
May 2020



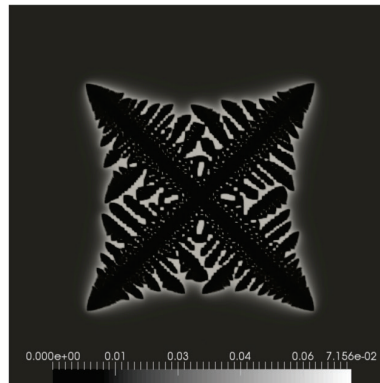
Phase-field( $\phi$ ); Isotropic  
( $\varepsilon(\theta) = \bar{\varepsilon}$ );  $\emptyset$ -Noise ( $\alpha = 0.0$ )



Con. Field ( $c$ ); Isotropic  
( $\varepsilon(\theta) = \bar{\varepsilon}$ );  $\emptyset$ -Noise ( $\alpha = 0.0$ )



Phase-field( $\phi$ ); Anisotropic  
( $\gamma = 0.05$ ); Noise ( $\alpha = 0.01$ )



Con. Field ( $c$ ); Anisotropic  
( $\gamma = 0.05$ ); Noise ( $\alpha = 0.01$ )

**The U.S. Army Engineer Research and Development Center (ERDC)** solves the nation's toughest engineering and environmental challenges. ERDC develops innovative solutions in civil and military engineering, geospatial sciences, water resources, and environmental sciences for the Army, the Department of Defense, civilian agencies, and our nation's public good. Find out more at [www.erdcl.usace.army.mil](http://www.erdcl.usace.army.mil).

To search for other technical reports published by ERDC, visit the ERDC online library at <http://acwc.sdp.sirsi.net/client/default>.

# **Phase-Field Simulations of Solidification in Support of Additive Manufacturing Processes**

Jeffrey B. Allen

*Information Technology Laboratory  
U.S. Army Engineer Research and Development Center  
3909 Halls Ferry Road  
Vicksburg, MS 39180-6199*

Robert D. Moser and Zachery B. McClelland

*Geotechnical and Structures Laboratory  
U.S. Army Engineer Research and Development Center  
3909 Halls Ferry Road  
Vicksburg, MS 39180-6199*

Jacob Kallivayalil and Arjun Tekalur

*Eaton Corportation, Plc.  
26201 Northwestern Highway  
Southfield, MI 48076*

Final report

Approved for public release; distribution is unlimited.

Prepared for U.S. Army Corps of Engineers  
Washington, DC 20314-1000

Under L32L43, "Additive Manufacturing"  
Program element number 0603734A  
Project number 479378.2  
Task number A1260

## Abstract

For purposes relating to force protection through advancements in multiscale materials modeling, this report explores the use of the phase-field method for simulating microstructure solidification of metallic alloys. Specifically, its utility was examined with respect to a series of increasingly complex solidification problems, ranging from one dimensional, isothermal solidification of pure metals to two-dimensional, directional solidification of non-isothermal, binary alloys. Parametric studies involving variations in thermal gradient, pulling velocity, and anisotropy were also considered, and used to assess the conditions for which dendritic and/or columnar microstructures may be generated. In preparation, a systematic derivation of the relevant governing equations is provided along with the prescribed method of solution.

**DISCLAIMER:** The contents of this report are not to be used for advertising, publication, or promotional purposes. Citation of trade names does not constitute an official endorsement or approval of the use of such commercial products. All product names and trademarks cited are the property of their respective owners. The findings of this report are not to be construed as an official Department of the Army position unless so designated by other authorized documents.

**DESTROY THIS REPORT WHEN NO LONGER NEEDED. DO NOT RETURN IT TO THE ORIGINATOR.**

# Contents

<b>Abstract</b> .....	<b>ii</b>
<b>Figures and Tables</b> .....	<b>iv</b>
<b>Preface</b> .....	<b>v</b>
<b>1 Introduction</b> .....	<b>1</b>
1.1 Background.....	1
1.2 Objective.....	2
<b>2 Model Derivation and Numerical Considerations</b> .....	<b>4</b>
2.1 Generalized theory and preliminary considerations .....	4
2.2 Generalized solidification equations: Isothermal binary alloys .....	4
2.3 Generalized solidification equations: Non-isothermal pure metals .....	8
2.4 Generalized solidification equations: Directional solidification of binary alloys.....	8
2.5 Techniques for numerical solution .....	9
<b>3 Material Properties and Thermophysical Data</b> .....	<b>12</b>
<b>4 Discussion and Results</b> .....	<b>13</b>
4.1 Nonisothermal pure metals .....	13
4.2 Isothermal binary alloys .....	15
4.2.1 Preliminary one-dimensional simulations.....	15
4.2.2 Two-dimensional simulations.....	17
4.3 Directional solidification of binary alloys .....	19
<b>5 Summary and Conclusions</b> .....	<b>23</b>
<b>References</b> .....	<b>24</b>
<b>Acronyms and Abbreviations</b> .....	<b>27</b>
<b>Report Documentation Page</b>	

# Figures and Tables

## Figures

Figure 1. Computational domain corresponding to directional solidification, showing direction of heat flow and imposed boundary conditions. ....	11
Figure 2. Time evolution of the phase-field $\phi$ , and temperature $T$ , for solidification of pure nickel.....	14
Figure 3. Phase-field contours of pure Ni at time $t=4.5E-8s$ showing the effect of increases in anisotropy and noise magnitude.....	15
Figure 4. Steady state interfacial concentration and phase-field profiles as a function of grid number for $T=870.0 K$ .....	17
Figure 5. Interfacial concentration showing the effect of variable interface velocity.....	17
Figure 6. Isothermal PFM contours of phase-field and concentration, contrasting isotropic interfacial energies (see (a) & (b)) and anisotropic energies (see (c) & (d)).....	19
Figure 7. Evolutionary contours of the phase-field ( $\phi$ ) for Al-2wt.%Si comparing the resulting microstructure for two different temperature gradients ( $V_P = 100.0 \mu m/s$ ).....	21
Figure 8. SDAS as a function of solidification time, showing the cube root dependency and agreement with theoretical values (Kattamis and Flemmings 1965).....	22

## Tables

Table 1. Thermophysical data for pure Ni (Kim et al. 1999).....	12
Table 2. Thermo-physical data for Dilute Al-2wt.%Si (Kim et al. 1999, Murray and McAllister 1984). ....	12

## Preface

This study was conducted for the Military Engineering Business Area under Project L32L43, “Additive Manufacturing.” The technical monitor was Dr. Robert D. Moser.

The work was performed by the Computational Analysis Branch (CAB) of the Computational Science and Engineering Division (CSED), U.S. Army Engineer Research and Development Center-Information Technology Laboratory (ERDC-ITL). At the time of publication, Dr. Jeffrey L. Hensley was the Branch Chief; Dr. Jerry R. Ballard, Jr. was the Division Chief; and Dr. Robert M. Wallace was the Technical Director for Engineered Resilient Systems (ERS). The Deputy Director of ERDC-ITL was Ms. Patti S. Duett and the Director was Dr. David A. Horner.

At the time of publication, COL Teresa A. Schlosser was the Commander of ERDC and Dr. David W. Pittman was the Director.

# 1 Introduction

## 1.1 Background

Additive technologies, including Selective Laser Melting (SLM) (Brandl et al. 2012), Laser Cladding (LC) (Fallah et al. 2010), Electron Beam Melting (EBM) (Chao et al. 2013), and others, have significantly influenced advancements in materials manufacturing processes. Their ubiquity, in terms of utilization and availability, along with the corresponding increase in related research publications has, in recent years, provided ample evidence to support their continued, perhaps unparalleled, growth (Arcella and Froes 2000; Gong et al. 2013; Wilkes et al. 2013; Heinel et al. 2007; Yan et al. 2007). However, because material performance is largely affected by the quality of its underlying microstructure, which can be difficult to control, additive technologies, particularly those involving metal alloys, have shown relatively limited capacity to produce high quality, reproducible products, with limited defects. Various processing parameters, related to heat transfer, solute transportation, and solidification all affect the evolution of the microstructure and influence the formation of these defects in terms of spatial as well as temporal dynamics. Clearly, an enhanced understanding of the solidification and microstructure evolution processes is required.

Possessing an intermediate, mesoscopic length scale (ranging from nanometers to microns) and linking the atomistic with the continuum, a material microstructure can be described as the spatial arrangement of the phases and possible defects that have different compositional and/or structural character. Microstructure evolution takes place to reduce the total free energy of the system, and may include contributions from bulk chemical free energy, interfacial energy, elastic strain energy, magnetic energy, electrostatic energy, etc.

Complementary to experimental studies, computer models of the evolving microstructure, particularly with respect to solidification and phase transformations, have also increased in number and provided important contributions to better understanding material behavior (Maxwell and Hellawell 1975; Wolfram 1984; Saito et al. 1988; Spittle and Brown 1989). In recent years, the Phase Field Model (PFM) has become one of the

computational methods of choice for solidification research. This is due to its use of field variables acting continuously across the interface, its ability to avoid the explicit tracking of the complex solid-liquid interface, and its implicit ability to determine interfacial microstructure.

The earliest models of PFM-based solidification focused on pure metals and involved the simulation of equiaxed, dendritic growth subject to a supercooled melt (Kobayashi 1993). Models involving the solidification of binary alloys have since been developed by a variety of researchers with increasing levels of complexity. For isothermal purposes, this includes the work conducted by Wheeler et al. (1992), Wheeler et al. (1993), Kim et al. (1998), and Kim et al. (1999), whose respective contributions are commonly referred to as the WBM and KKS models; the latter being equivalent in all respects to the former, with the important exception of including an improved definition for the free energy density at the interfacial region. For non-isothermal solidification (involving complementary solutions from the energy equation), temperature effects are considered resulting from the latent heat release at the solid-liquid interface. Several researchers have examined this effect on pure and binary alloys, including the works of Conti (1997) and Loginova et al. (2001).

## 1.2 Objective

In this work, the solidification of pure Ni and a dilute Al-2wt.% Si alloy are investigated using the PFM developed by Kim et al. (1998, 1999). Unlike other models, such as Wheeler et al. (1992, 1993), this method was selected due to its ability to reliably reproduce interfacial energies for diffuse interface conditions. Microstructure simulations are performed assuming both isothermal and directional solidification and used to investigate dendritic evolution. While a large number of PFM based studies have focused on isothermal solidification of binary alloys, relatively few have been used to examine directional solidification, which, for example, can be used to quantify Secondary Arm Spacing (SDAS). Quantitative assessments of SDAS is important for a variety of reasons, which include the determination of micro-segregation patterns, overall material strength in additive manufacturing (i.e. laser deposition processes) (Ghosh et al. 2017), and the prediction of cooling rates within cast alloys (Ode et al. 2001).

This work commences with a statement of the free energy functional and corresponding free energy density as prescribed by Kim et al. (1998, 1999). The governing evolution equations relevant to phase and composition are then presented, with anisotropy included as part of the interfacial gradient energy. These are supplemented by various interpolation functions and other phase-field parameters that are derived from the thin interface limit (Kim et al. 1998), and include the implications due to the assumption of chemical equilibrium within the interface. Directional solidification, involving the use of a spatial temperature gradient is also considered.

## 2 Model Derivation and Numerical Considerations

### 2.1 Generalized theory and preliminary considerations

As prescribed by Kim et al. (1998, 1999) and in conformance with the dilute interface assumption, the phase-field  $\phi(x, y, t)$  is used to indicate the physical state of the system at each point within a computational domain. The solid and liquid states are represented by  $\phi = 1$  and  $\phi = 0$ , respectively, while the interface is represented by a thin, but smooth transition layer ( $0 < \phi < 1$ ) that serves to replace the classical, discontinuous, sharp interface theory (Caginalp 1993). According to the Landau-Ginzburg theory (Hohenberg and Krekhov 2015), and excluding contributions from crystallographic orientation, the total energy functional, defined over a spatial domain ( $\Omega$ ), may be expressed as:

$$F = \int \left[ \frac{\varepsilon^2}{2} |\nabla\phi|^2 + f(\phi, c, T) \right] d\Omega \quad (1)$$

where  $c(x, y, t)$ ,  $\phi(x, y, t)$ ,  $T(x, y, t)$ , and  $\varepsilon(\theta)$  are variables representing the concentration, phase-field, temperature, and gradient energy, respectively. Since a binary material is assumed,  $1 - c(x, y, t)$  represents the composition of the second species. Minimizing this total free energy results in the thermodynamically consistent evolution of the phase-field and the concentration, which may be expressed as:

$$\frac{\partial\phi}{\partial t} = -M \frac{\delta F}{\delta\phi} = M(\nabla \cdot \varepsilon^2 \nabla\phi^2 - f_\phi(\phi, c, T)) \quad (2)$$

$$\frac{\partial c}{\partial t} = \nabla \cdot \left[ \frac{D(\phi)}{f_{cc}} \nabla f_c \right] \quad (3)$$

with  $M$  representing the mobility of the interface kinetics (to be defined later), and  $D(\phi)$  the chemical diffusivity, assumed as:  $D(\phi) = h(\phi)D_S + (1 - h(\phi))D_L$  (Kim et al. 1998, 1999).

### 2.2 Generalized solidification equations: Isothermal binary alloys

For isothermal binary alloys, the free energy density,  $f(c, \phi)$ , shown in the second term of Equation (1) may be expressed by the mixture rule, comprised of the solid and liquid energies along with a double well potential,  $wg(\phi)$ :

$$f(\phi, c) = h(\phi)f^S(c_S) + (1 - h(\phi))f^L(c_L) + wg(\phi) \quad (4)$$

where  $f^S$  and  $f^L$  represent the free energies associated with the solid and liquid phases, respectively, and  $w$  is the height of the imposed interfacial potential.  $h(\phi)$  is some interpolating, monotonic polynomial satisfying  $h(0) = 0$  and  $h(1) = 1$  (i.e., in this work  $h(\phi) = \phi^3(10 - 15\phi + 6\phi^2)$ ), and  $g(\phi)$  is a double well potential, given as:

$$g(\phi) = 4\phi^3 - 6\phi^2 + 2\phi \quad (5)$$

The phase-field parameters,  $\varepsilon_0$  and  $w$ , are related to the interface energy,  $\sigma$ , and interface width  $2\lambda$ , (defined within the interval:  $0.1 \leq \phi \leq 0.9$ ). It may be found from 1D solutions of the equilibrium phase-field equation (Kim et al. 1999):

$$\sigma = \frac{\varepsilon_0 \sqrt{w}}{3\sqrt{2}} \quad (6)$$

$$2\lambda = 2.2\sqrt{2} \frac{\varepsilon_0}{\sqrt{w}} \quad (7)$$

The mobility is given by the thin interface limit conditions (Ferreira et al. 2015):

$$M^{-1} = \frac{\varepsilon^2}{\sigma\sqrt{2w}} \left( \frac{1}{D_L} \xi(c_S^e, c_L^e) \right) \quad (8)$$

$$\xi(c_S^e, c_L^e) = \frac{RT}{v_m} (c_L^e - c_S^e)^2 \int_0^1 \frac{h(\phi)(1-h(\phi))}{(1-h(\phi))c_L^e(1-c_L^e) + h(\phi)c_S^e(1-c_S^e)} \frac{d\phi}{\sqrt{g(\phi)}} \quad (9)$$

The effect of anisotropy is given by:

$$\varepsilon(\theta) = \bar{\varepsilon}(1 + \gamma \cos v(\theta - \theta_0)) \quad (10)$$

where  $\bar{\varepsilon}$ ,  $\gamma$ , and  $v$  are constants describing the magnitude of the gradient energy, the anisotropy, and the mode number, respectively. The mode number is used to describe symmetry, with  $v = 0$  (isotropic),  $v = 4$  (quadrilateral),  $v = 6$  (hexagonal), etc. The angle  $\theta$  is the orientation of the normal to the interface with respect to the horizontal ( $x$ ) axis, and is given by:  $\tan\theta = (\partial\phi/\partial y)/(\partial\phi/\partial x)$ , and  $\theta_0$  is a constant referring to the initial orientation offset.

Following the KKS model (Kim et al. 1999), the equality of the chemical potential for both phases,  $S$  and  $L$  (Equation 14), and the definition of the free energy density (Equation 4), allows for the equation:

$$\frac{\partial f}{\partial \phi} = h'(\phi)(f^S(c_S) - f^L(c_L)) + wg'(\phi) + h(\phi)\mu \frac{\partial c_S}{\partial \phi} + (1 - h(\phi))\mu \frac{\partial c_L}{\partial \phi} \quad (11)$$

Since the concentration,  $c$ , is independent of  $\phi$ , the equation is:

$$h(\phi) \frac{\partial c_S}{\partial \phi} + (1 - h(\phi)) \frac{\partial c_L}{\partial \phi} = \frac{\partial c}{\partial \phi} - h'(\phi)(c_S - c_L) = -h'(\phi)(c_S - c_L) \quad (12)$$

therefore,

$$\frac{\partial f}{\partial \phi} = -h'(\phi)(f^L(c_L) - f^S(c_S) - \mu(c_L - c_S)) + wg'(\phi) \quad (13)$$

The following equation is derived from substituting Equation 13 into Equation 2 and assuming isothermal conditions.

$$\frac{1}{M} \frac{\partial \phi}{\partial t} = \nabla \cdot \varepsilon^2 \nabla \phi + h'(\phi)[f^L(c_L) - f^S(c_S) - \mu(c_L - c_S)] - wg'(\phi) \quad (14)$$

Applying the dilute solution limit, the thermodynamic driving force  $G(c_S, c_L)$  can be approximated as (Kim et al. 1999):

$$G(c_S, c_L) \equiv f^L(c_L) - f^S(c_S) - (c_L - c_S)f_{c_L}^L(c_L) = \frac{RT}{v_m} \ln \frac{(1-c_S^e)(1-c_L)}{(1-c_L^e)(1-c_S)} \quad (15)$$

Thus,

$$\frac{1}{M} \frac{\partial \phi}{\partial t} = \nabla \cdot \varepsilon^2 \nabla \phi + h'(\phi)G(c_S, c_L) - Wg'(\phi) \quad (16)$$

Finally, applying the effects due to anisotropy (Equation 10), we arrive at:

$$\begin{aligned} \frac{1}{M} \frac{\partial \phi}{\partial t} = \nabla \cdot (\varepsilon(\theta)^2 \nabla^2 \phi) + \frac{\partial}{\partial y} \left( \varepsilon(\theta) \varepsilon'(\theta) \frac{\partial \phi}{\partial x} \right) - \frac{\partial}{\partial x} \left( \varepsilon(\theta) \varepsilon'(\theta) \frac{\partial \phi}{\partial y} \right) - wg'(\phi) + \\ \frac{RT}{v_m} h'(\phi) \ln \left( \frac{1-c_S^e}{1-c_L^e} \frac{1-c_L}{1-c_S} \right) \end{aligned} \quad (17)$$

The concentration equation is obtained similarly, but for the sake of brevity it is expressed as:

$$\frac{\partial c}{\partial t} = \nabla \cdot \left[ D(\phi) \{ (1 - h(\phi))c_L(1 - c_L) + h(\phi)c_S(1 - c_S) \} \nabla \ln \frac{c_L}{1 - c_L} \right] + \nabla \cdot \alpha_i \frac{\partial \phi}{\partial t} \frac{\nabla \phi}{|\nabla \phi|}. \quad (18)$$

Where the last term on the right-hand side of Equation 18 represents the anti-trapping flux term, with  $\alpha_i = \frac{\varepsilon}{\sqrt{2W}}(c_L - c_S)$ , and  $\varepsilon$ ,  $W$  representing the square root of the energy gradient and the height of the energy barrier associated with the interface, respectively.

Note the approximation for the thermodynamic driving force  $G(c_S, c_L)$ , precludes the necessity for obtaining explicit formulas for  $f^L(c_L)$  and  $f^S(c_L)$ . Although these are often obtained from parabolic functions whose first and second derivatives are imported from thermodynamic databases (Zho et al. 2004), the assessment of the equilibrium and non-equilibrium concentrations for each phase is still required. While the former may be obtained, for a given initial concentration, from standard equilibrium phase diagrams, the latter may be obtained using the dilute assumption.

Following the proposed model of Kim et al. (1998, 1999), auxiliary variables  $c_S$  and  $c_L$  are introduced describing the composition of the solid and liquid phases, respectively. To solve for these variables, the total concentration,  $c$ , is expressed as a fraction-weighted combination as shown in Equation 19.

$$c = h(\phi)c_S + (1 - h(\phi))c_L. \quad (19)$$

Additionally, the concentrations are constrained so the solid and liquid fractions could, at any point in the interface, satisfy equal chemical potentials, according to:

$$\mu^S(c_S) = \mu^L(c_L) = \frac{\partial f^S(c_S)}{\partial c} = \frac{\partial f^L(c_L)}{\partial c}. \quad (20)$$

In the absence of explicit forms for  $f^S(c_S)$  and  $f^L(c_L)$  (see for example the HBSM model (Hu et al. 2007), under the dilute assumption (Kim et al. 1998), Equation 20 may be simplified as:

$$\frac{c_S^e c_L}{c_L^e c_S} = \frac{(1 - c_S^e)(1 - c_L)}{(1 - c_L^e)(1 - c_S)} \quad (21)$$

Equations 19 and 21 may then be used to compute the liquid and solid concentrations.

Finally, to stimulate fluctuations at the dendrite interface, a noise correction factor may be appended to the phase-field equation (Ferreira et al. 2015):

$$noise = 16.0g(\phi)\alpha r \quad (22)$$

where  $r$  is a random number between +1 and -1, and  $\alpha$  represents the amplitude of the fluctuation.

### 2.3 Generalized solidification equations: Non-isothermal pure metals

For pure metals, the concentration ( $c$ ) becomes a constant (i.e.  $\frac{\partial c}{\partial t} = 0$ ).

Therefore, the time evolution of the phase-field only has to be considered, which is given by:

$$\frac{1}{M} \frac{\partial \phi}{\partial t} = \nabla \cdot (\varepsilon(\theta)^2 \nabla \phi) + \frac{\partial}{\partial y} \left( \varepsilon(\theta) \varepsilon'(\theta) \frac{\partial \phi}{\partial x} \right) - \frac{\partial}{\partial x} \left( \varepsilon(\theta) \varepsilon'(\theta) \frac{\partial \phi}{\partial y} \right) - wg'(\phi) - \frac{\Delta H}{T_m} h'(\phi)(T - T_m) \quad (23)$$

where  $T_m$  and  $\Delta H$  are the melting temperature and latent heat, respectively. For a non-uniform temperature field, Equation 23 is accompanied by an energy transport equation of the form;

$$\frac{\partial T}{\partial t} = D \nabla^2 T + \frac{\Delta H}{\rho C_p} h'(\phi) \quad (24)$$

where  $D$  is the thermal diffusivity,  $\rho$  is the density, and  $C_p$  is the specific heat.

### 2.4 Generalized solidification equations: Directional solidification of binary alloys

Finally, the case of directional solidification was investigated. In this case, the evolution equations shown previously were modified in order to accommodate an evolving temperature field that varies in both time and space. While details concerning their formulation are provided in Ohno and Matsuura (2009), Sakane et al. (2015), and Echebarria et al. (2004), for purposes of economy, only the resulting evolution equations are provided:

$$\tau[1 - (1 - k)u'] \frac{\partial \phi}{\partial t} = \nabla \cdot (\varepsilon(\theta)^2 \nabla^2 \phi) + \frac{\partial}{\partial y} \left( \varepsilon(\theta) \varepsilon'(\theta) \frac{\partial \phi}{\partial x} \right) - \frac{\partial}{\partial x} \left( \varepsilon(\theta) \varepsilon'(\theta) \frac{\partial \phi}{\partial y} \right) + \phi - \phi^3 - \lambda^*(1 - \phi^2)^2(u - u') \quad (25)$$

$$\frac{1}{2}[1 + k - (1 - k)\phi] \frac{\partial u}{\partial t} = \nabla[D_l q(\phi)\nabla u - j_{at}] + \frac{1}{2}[1 + (1 - k)u] \frac{\partial \phi}{\partial t} \quad (26)$$

$$T(x) = T_0 + G(x - V_p t) \quad (27)$$

where  $T_0$  is the reference temperature at  $x = 0$  and  $t = 0$ ,  $G$  is the temperature gradient,  $x$  is the spatial coordinate along the gradient direction, and  $V_p$  is the pulling velocity. The variable  $u$  is the non-dimensional concentration defined as:  $u = (c_l - c_l^e)/(c_l^e - c_s^e)$ , and the relaxation time,  $\tau = \tau_0(1 + \gamma \cos v(\theta))$ , where  $\tau_0 = a_2 \lambda^* W_0^2 / D_l$  (with  $a_2 = 0.6267$ ). Additionally,  $u' = (x - V_p t) / [\frac{|m|(1-k)c_0}{kG}]$ ,  $q(\phi) = [kD_s + D_l + (kD_s - D_l)\phi] / (2D_l)$ ,  $a_1 = 0.88388$ , and the capillary length,  $d_0 = k\Gamma / (|m|(1 - k)c_0)$ . The anti-trapping current,  $j_{at}$ , was included in order to reduce artificial solute trapping. Proportional to the interface thickness ( $W_0$ ) and growth velocity ( $\frac{d\phi}{dt}$ ),  $j_{at}$  is directed from the solid to the liquid in order to assist in solute redistribution, and was defined as (Echebarria et al. 2004; Takaki et al. 2016);

$$j_{at} = -\frac{(1 - k \frac{D_s}{D_l})}{2\sqrt{2}} W_0 [1 + (1 - k)u] \left( \frac{d\phi}{dt} \right) \nabla \phi / |\nabla \phi| \quad (28)$$

## 2.5 Techniques for numerical solution

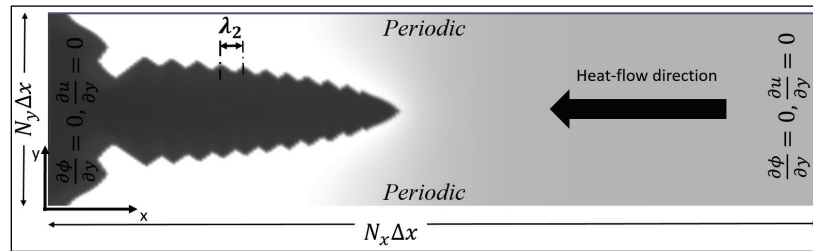
The model equations were solved using Finite Difference (FD) approximations, with second order, central differences applied to all spatial discretizations, and first order (explicit), forward Euler discretizations (Euler 1768) used to advance the time step. While any number of solution/discretization methods are applicable, including the Finite Element (FE), Finite Volume (FV), or Fourier Spectral (FS) methods, use of the FD technique was based primarily on its relative simplicity and straightforward manner for discretizing the governing equations and implementing the boundary conditions. Further, while it is true that the KKS method (Kim et al. 1998, 1999) consists in solving a system of non-linear coupled partial differential equations, the simplifications assumed in this work, in particular the dilute assumption (Kim et al. 1998), render the equations solvable via the explicit Euler

technique. Of course, the downside is that for stability purposes, there is the requirement to utilize a relatively small time step in accordance with  $\Delta t < \Delta x^2 / 4D_L$ . (where  $\Delta x$  is the grid resolution; itself dependent on the desired interface resolution).

Additionally, the traditional five point stencil (2<sup>nd</sup> order accuracy) was imposed for the discretization of the diffusion operator (in Equations 11 and 12) in lieu of a 9 point stencil (with 4<sup>th</sup> order accuracy). Although the use of the 9-point stencil would serve to improve convergence accuracy, its use would not necessarily serve to mitigate the so called effects of “mesh-induced anisotropy,” which can be particularly problematic for dendritic solidification of alloy materials involving solute transport. Various studies have shown that mesh-induced anisotropy can be mitigated, to some degree, by substantially increasing the grid resolution within the evolving liquid/solid interface region (Mullis 2006). In the simulations, in addition to the inclusion of several grid points within the interface region, its potential influence (for the isothermal cases) was attempted to be offset by rotating  $\theta_0$  by 45 degrees ( $\varepsilon(\theta) = \bar{\varepsilon}(1 + \gamma \cos k(\theta - \theta_0))$ ). This ensured the growth directions would not lie along the horizontal and vertical axes (associated with the strongest potential for mesh-induced anisotropy).

According to the specific case, the boundary conditions were designated as either zero-flux conditions (i.e.,  $\partial\phi/\partial y = 0, \partial c/\partial y = 0$ ) or periodic (Figure 1 illustrates the conditions corresponding to directional solidification). The initial conditions, typically consisted of a solid seed embedded within a uniform liquid region. The grid resolution ( $\Delta x = \Delta y$ ) was designated sufficiently small in order to accommodate several grid points within the interface region; the thickness of which as designated by Equation 7. For stability and convergence purposes, the time step was approximated by:  $\Delta t = 0.25 * \Delta x^2 / D_L$ , and the domain size varied according to the case. All other relevant parameters, including material property and thermo-physical data, shown in Tables 1 and 2. Algorithm development was performed using FORTRAN 90, and the simulations were run on a 64 bit LINUX machine with an Intel Xeon processor (1.86 GHz, 7.8 GB RAM).

Figure 1. Computational domain corresponding to directional solidification, showing direction of heat flow and imposed boundary conditions.



### 3 Material Properties and Thermophysical Data

The thermo-physical properties for each of the three material cases, corresponding to pure nickel (Ni) and Aluminum silicon alloy (Al-2wt.%Si) are shown in Tables 1 and 2.

**Table 1. Thermophysical data for pure Ni (Kim et al. 1999).**

Anisotropy constant, $\gamma$	0.025
Noise Amplitude, $\alpha$	0.025
Time step, $\Delta t$	1.0E-12 (s)
Grid Spacing, ( $\Delta x = \Delta y$ )	2.0E-8 (m)
Gradient energy, $\bar{\epsilon}$	2.01E-4 ( $J/m^3$ ) <sup>1/2</sup>
Mobility, $M_\phi$	13.47 ( $m^3/s \cdot J$ )
Free energy factor, $W$	0.61E8 ( $J/m^3$ )
Latent heat, $L$	2.35E9 ( $J/m^3$ )
Thermal Diffusivity, $D$	1.55E-5 ( $m^2/s$ )
Specific heat, $c_p$	5.42E6 ( $J/m^3 \cdot K$ )
Interface energy, $\sigma$	0.37 ( $J/m^2$ )
Melting temperature, $T_m$	1728 (K)
Linear kinetic coeff., $\beta$	2.0 ( $m/(K \cdot s)$ )
Interface Thickness, $\delta$	4.0E-8 (m)

**Table 2. Thermo-physical data for Dilute Al-2wt.%Si (Kim et al. 1999, Murray and McAllister 1984).**

Diffusion coefficient in solid, $D_S$	1.0E-12 $m^2/s$
Diffusion coefficient in liquid, $D_L$	3.0E-9 $m^2/s$
Melting temperature, $T_M$	933.6 K
Molar Volume, $V_m$	1.06E-5 $m^3/mol$
Interface energy, $\sigma$	0.093 $J/m^2$
Partition coefficient, $k$	0.12 (@ 870 K)
Liquidus slope, $m$	-6.5 K/wt.%
Gibbs-Thomson constant, $\Gamma$	1.60 x 10 <sup>-7</sup> K*m
Anisotropic strength, $\gamma$	0.02
Reference Temperature, $T_0$	870 K
Temperature Gradient, $G$	80E3 K/m & 120E3 K/m
Pulling Velocity, $V_p$	

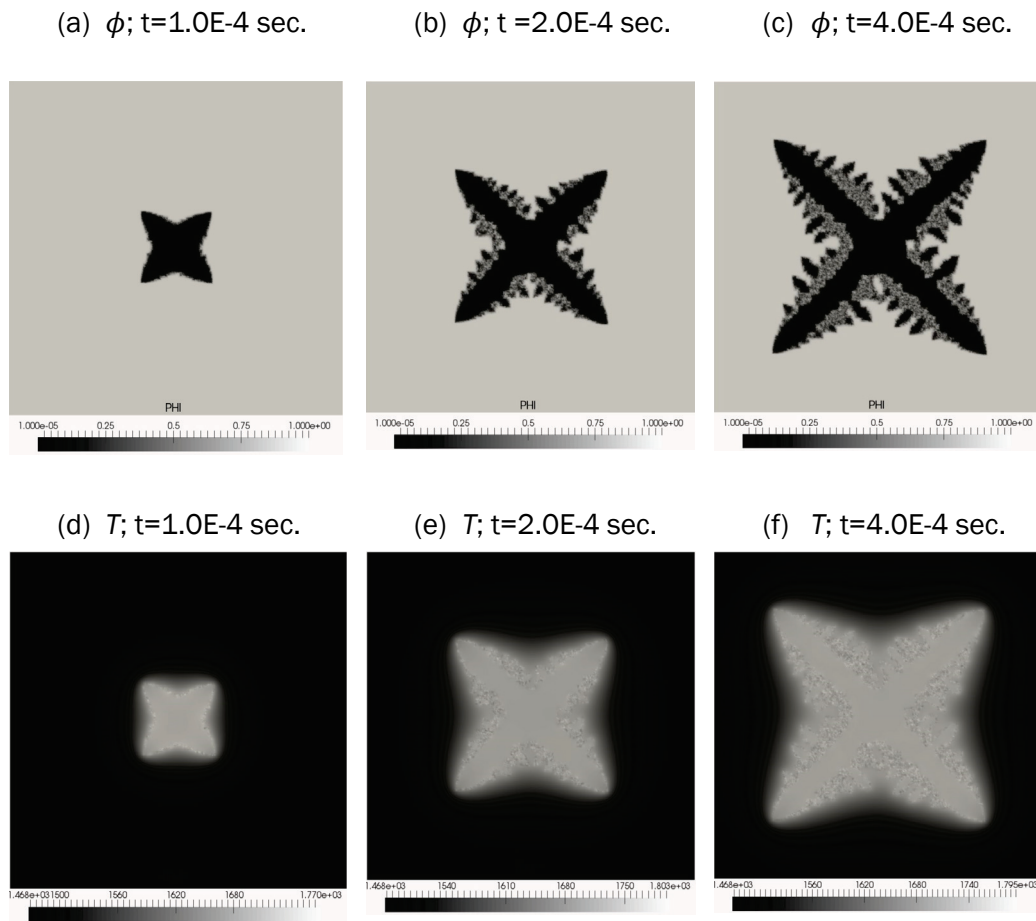
## 4 Discussion and Results

### 4.1 Nonisothermal pure metals

The parameters used in this first case correspond to pure nickel and are shown in Table 1. The interface thickness, ( $\delta = 2\Delta x$ ), was selected in accordance with the sharp interface morphological stability condition (Kim et al. 1998), and the domain resolution of  $400 \times 400$  thus corresponded to a size,  $X = Y = 8\mu m$ . Initialization conditions included undercooling of the nickel melt to  $0.6L/c_p$ , the assignment of a solid seed, (of size  $\Delta x \Delta y$  placed at the center of the domain), to  $\phi = 0$ , and the remaining liquid with the assignment  $\phi = 1$ . Additionally, an initial reference angle,  $\theta_0 = \pi/4$  (used within Equation 10) was imposed in order to preferentially facilitate maximum dendritic growth along the  $[\bar{1}01]$  and  $[0\bar{1}1]$  directions. All other conditions, including boundary and noise conditions, were assigned in accordance with those previously specified.

Figure 2 shows the contour results corresponding to the evolution of the phase-field and temperature over a time interval of  $4.0E-4$  s. In this case, due to the specification of the initial reference angle ( $\theta_0 = \pi/4$ ), the primary dendritic arms evolve along the  $[\bar{1}01]$  and  $[0\bar{1}1]$  directions. As indicated, and in accordance with previous results (Kim et al. 1999; Ferreira et al. 2015), the parabolic, dendrite tips evolve along the directions of maximum interface energy. Secondary branches, extending perpendicularly to the primary arms, also become noticeable at approximately  $t = 2.0E - 4$  s. The contours of temperature further mimic the phase-field dendritic pattern, but suffuse to greater circumambient regions.

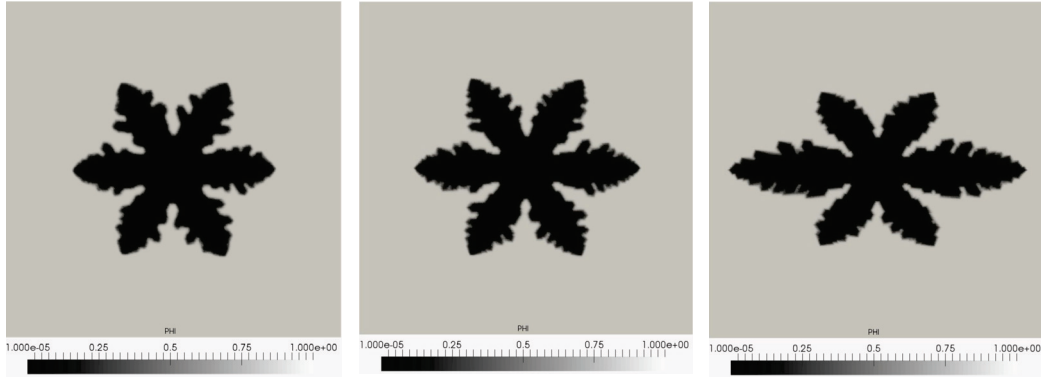
Figure 2. Time evolution of the phase-field  $\phi$ , and temperature  $T$ , for solidification of pure nickel.



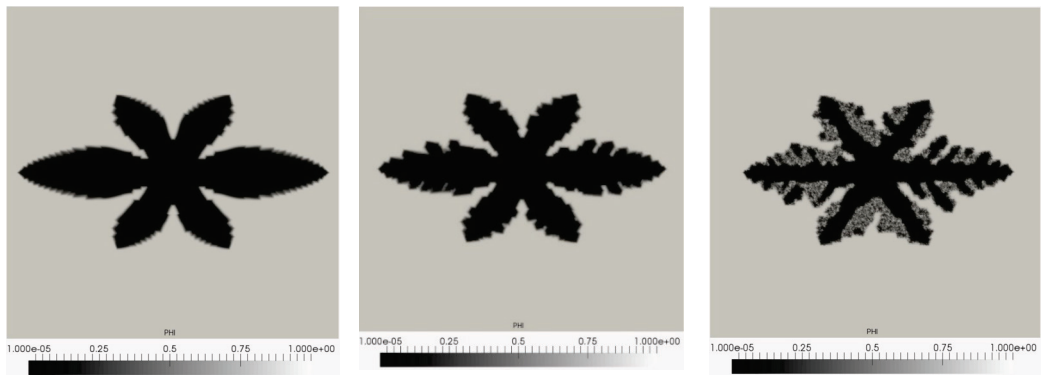
In Figure 3, the effects due to changes in anisotropy (Figure 3a-3c) and noise (Figure 3d-3f) are illustrated for a dendrite structure at time,  $t=4.5E-8$  seconds with hexagonal symmetry. That is,  $\nu = 6$  in Equation 10, (the primary dendrite arms are inclined at  $60^\circ$  relative to each other), and the growth is along the  $\langle 110 \rangle$  crystallographic orientations. For a constant noise ( $\alpha = 0.01$ ), and anisotropy increasing from  $\gamma = 0.01$  to  $\gamma = 0.067$ , it is seen that the number and magnitude of the lateral, secondary dendritic braches become more developed. Their direction evolves as well, tending initially to develop perpendicularly to the main branch, while later tending to become more aligned. The overall shape of the primary structure tends to elongate as well, along the  $[\bar{1}10]$  and  $[1\bar{1}0]$  directions. As indicated in Figure 3d-3f, the effect of increased noise results in a significant increase in secondary dendritic structures.

Figure 3. Phase-field contours of pure Ni at time  $t=4.5E-8s$  showing the effect of increases in anisotropy and noise magnitude.

(a)  $\alpha = 0.01 ; \gamma = 0.01$       (b)  $\alpha = 0.01 ; \gamma = 0.025$       (c)  $\alpha = 0.01 ; \gamma = 0.067$



(d)  $\gamma = 0.067 ; \alpha = 0.0$       (e)  $\gamma = 0.067 ; \alpha = 0.01$       (f)  $\gamma = 0.067 ; \alpha = 0.025$



## 4.2 Isothermal binary alloys

### 4.2.1 Preliminary one-dimensional simulations

Preliminarily, one dimensional, steady-state, simulations were performed of Al-2wt.% Si at 870K. The simulations were performed over 1,000 grid points using a resolution of  $\Delta x = 0.5nm$ . The relevant thermo-physical properties are shown in Table 2, with equilibrium solid and liquid compositions of 0.006387 and 0.079, respectively (Kim et al. 1998). Solutions were obtained by solving Equation 17 and Equation 18 (along the x-direction) utilizing no-flux boundary conditions ( $\partial\phi/\partial x = 0, \partial c/\partial x = 0$ ) for both the concentration and phase-field. Initial conditions consisted of a constant temperature, undercooled system (with:  $T_{sol} < T < T_{liq}$ ), and a solid phase nucleating particle located at one end of the system with the

same composition as the bulk liquid. The interface thickness ( $2\lambda$ ) was prescribed as 3.0 nm, thus offering an interface resolution of six grid points. In accordance with Kim et al. (1998), in order to guarantee the existence of a steady-state solution, a solute sink was placed at some specified distance from the interface. At each time step, the solute sink was moved by the interface migration distance and was forced to assume the initial bulk composition. Using this method, the interface velocity (at the steady state) could be varied by changing the distance between the solute sink and the interface. In most cases, the system was observed to reach a steady state after a transient period of approximately  $1.0 \times 10^6$  time steps (with  $\Delta t < \Delta x^2/4D_L$ ), and corresponded to a total computational (CPU) time of approximately 10 min.

Figure 4 shows the steady-state phase-field and concentration profiles at the interface for a temperature of 870K and an interface velocity of 0.043 m/s. As indicated, the concentration reaches a maximum of approximately 0.08 (approximately equivalent to the equilibrium liquid composition), and reaches this peak near the leading edge of the interface. Further, it is noted that the interface thickness over which the phase-field changes from 0.1 to 0.9 conforms to the prescribed interface grid resolution.

In Figure 5, the effects on concentration due to an increasing interface velocity is shown. As mentioned previously, variable velocities were achieved by varying the prescribed distance between the interface (i.e.,  $\phi = 0.5$ ) and the solute sink. As indicated, velocities of 0.043 m/s and 0.17 m/s were investigated. Note that interface velocities,  $V$ , were chosen so the thin interface limit was preserved (i.e.,  $\ll D_L/V$ ) (Kim et al. 1999). Consistent with previous findings (Kim et al. 1998, 1999), the results indicate a decrease in the maximum concentration for larger interface velocities. At lower interface velocities, more solute is able to diffuse into the liquid phase resulting in higher maximum concentrations, while at higher velocities lower concentrations are observed due to the effects of solute trapping.

**Figure 4. Steady state interfacial concentration and phase-field profiles as a function of grid number for  $T=870.0$  K.**

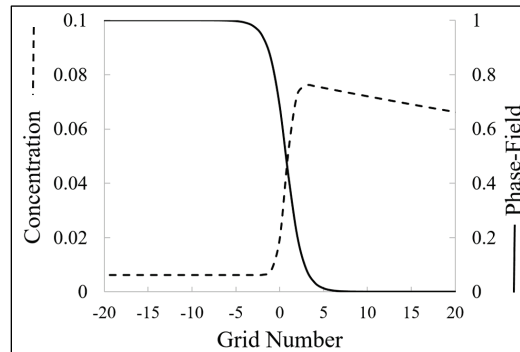
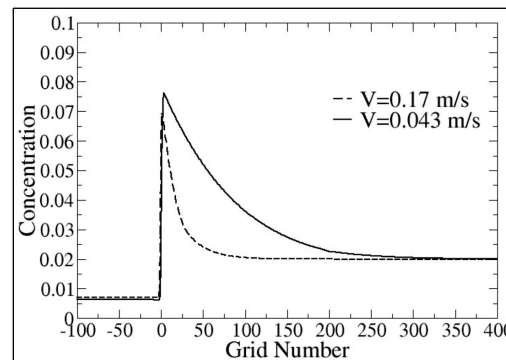


**Figure 5. Interfacial concentration showing the effect of variable interface velocity.**



#### 4.2.2 Two-dimensional simulations

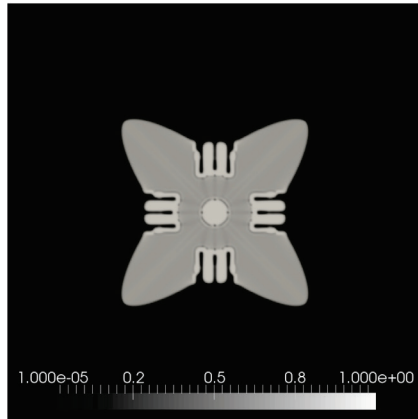
Next, the results for two dimensional, steady-state, solidification simulations of binary Al-Si alloys over a computational domain of  $8\mu m$  by  $8\mu m$  ( $400 \times 400$  grid points) are presented. As done previously, all relevant thermo-physical properties were taken from Table 2 with mixed periodic and zero-flux boundary conditions ( $\partial\phi/\partial x = 0$ ,  $\partial c/\partial x = 0$ ) prescribed in accordance with Figure 1. As before, the initial conditions consisted of a solid phase, undercooled nucleating seed (with:  $T_{sol} < T < T_{liq}$ ) with an equivalent composition to the bulk liquid. In this first case, assume isothermal conditions with initial composition Al-2wt.%Si and locate the nucleating seed at the center of the computational domain;  $X = 4\mu m$ ;  $Y = 4\mu m$ . Anisotropy was included as part of the interfacial energy in accordance with Equation 10 (with  $\epsilon = 0.05$ ;  $\theta_0 = 45^\circ$ ; and  $\nu = 4$ ), and noise was amended to the phase-field equation per Equation 22 (with  $\alpha = 0.01$ ) in order to stimulate additional interfacial growth. The interface thickness ( $2\lambda$ ) and grid resolution ( $\Delta x$ ) were prescribed as  $40.0 nm$  and  $20.0 nm$ , respectively. A time step of  $1.0 ns$  was used to run the simulations over a

total time of  $50 \mu s$  and (for the isotropic case) this required a total CPU time of 1.6 hr.

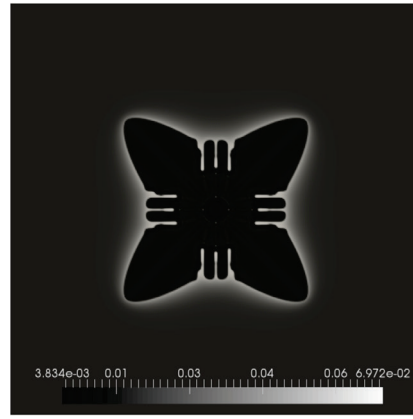
Figure 6 shows the isothermal phase-field and concentration contours for a temperature of 870K. Figure 6(a) and Figure 6(b) show the effects of assuming isotropic conditions (with  $\varepsilon(\theta) = \bar{\varepsilon}$ ) and zero-noise, while Figure 6(c) and Figure 6(d) show the effects of including anisotropic interfacial energy (with  $\gamma = 0.05$ ) and interfacial noise (with  $\alpha = 0.01$ ). The simulations were run for  $50 \mu s$  ( $\Delta t = 1.0 ns$ ), with the interface velocity for the isotropic case measured at 0.06 m/s. For each case, due to the specification of the initial reference angle ( $\theta_0 = \pi/4$ ), the primary, dendritic arms evolve along the  $\langle 1 1 0 \rangle$  directions (excluding the  $z$  coordinate), which correspond to the paths of maximum interface energy. The isotropic as well as the anisotropic results reveal the presence of well-defined, parabolic tips extending along the primary directions, but are clearly distinguished by the fact that the anisotropic model tends to create relatively narrow arms with sharper tips. Additionally, as opposed to the isotropic case, Figure 6(c) and Figure 6(d) clearly show the evidence of secondary and tertiary dendritic arm structure and serve to emphasize the impact of including anisotropy and noise within the simulations. The concentration contours shown in Figure 6(b) and Figure 6(d) further mimic the overall phase-field dendritic patterns and reveal the evolution of the solid phase, with maximum concentrations located along the  $\langle 1 0 0 \rangle$  directions, for the isotropic and anisotropic cases, respectively.

**Figure 6. Isothermal PFM contours of phase-field and concentration, contrasting isotropic interfacial energies (see (a) & (b)) and anisotropic energies (see (c) & (d)).**

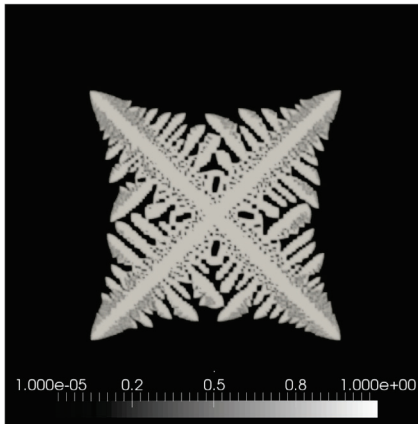
(a) Phase-field( $\phi$ ); Isotropic  
( $\varepsilon(\theta) = \bar{\varepsilon}$ );  $\phi$ -Noise ( $\alpha = 0.0$ )



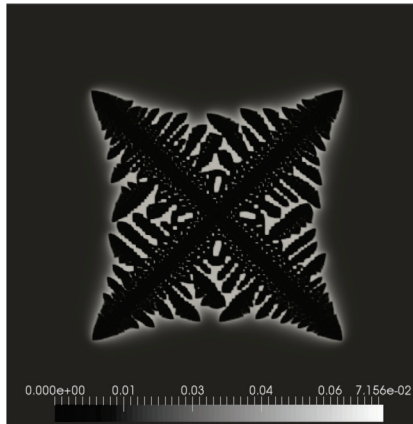
(b) Concentration Field( $c$ ); Isotrop.  
( $\varepsilon(\theta) = \bar{\varepsilon}$ );  $\phi$ -Noise ( $\alpha = 0.0$ )



(c) Phase-field( $\phi$ ); Aniso.  
( $\gamma = 0.05$ ); Noise ( $\alpha = 0.01$ )



(d) Concentration Field( $c$ ); Aniso.  
( $\gamma = 0.05$ ); Noise ( $\alpha = 0.01$ )



### 4.3 Directional solidification of binary alloys

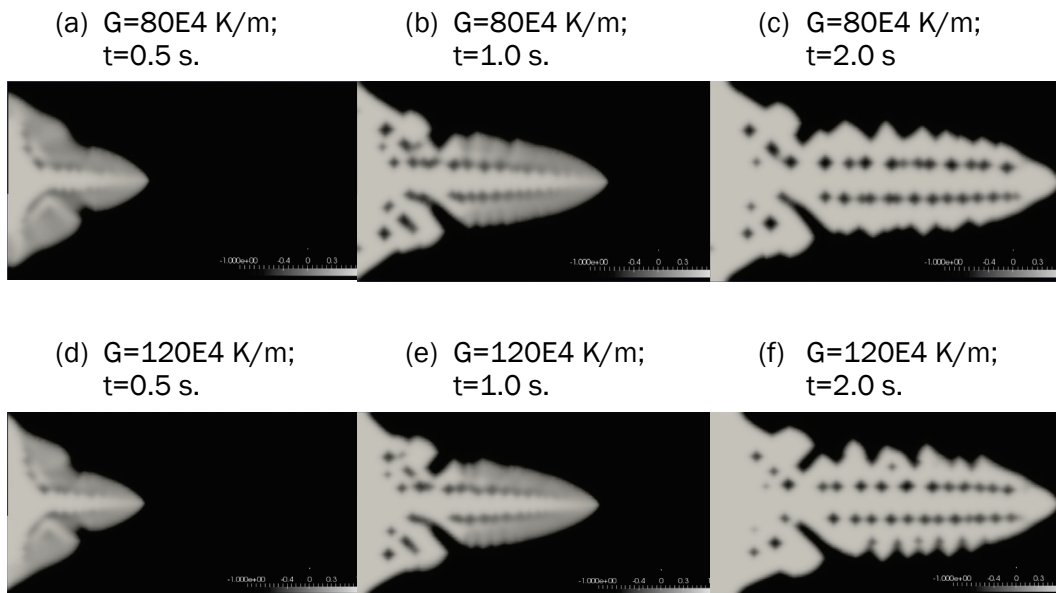
Directional solidification simulations of dilute binary alloys (i.e., Al-2wt.% Si) require evolutionary equations that accommodate an evolving temperature field as shown in Equations 25-27. As done previously, the addition of stochastic noise is included and appended to Equation 25. It has been observed that the dynamics of side-branching can be initiated by the inclusion of noise (Peters and Langer 1986; Brener and Temkin 1995). In this work, noise was introduced at the interface using a Gaussian form with amplitudes ranging from  $-d\phi$  to  $+d\phi$  and mean  $d\phi = 0$ .

For this report, and in accordance with the thin-interface limit analysis, the convergence of the simulation results is ensured by assigning an adequately small magnitude for the non-dimensional interface thickness ( $W_0/d_0$ ) (Echebarria 2004). Since  $\frac{W_0}{d_0} = \lambda/a_1$ , a proper assignment of the interface thickness, renders the simulation results reasonably independent of  $\lambda$ . In this work, and according to previous theoretical analyses (Mullins and Sekerka 1964),  $\lambda = 10.0$  ( $\frac{W_0}{d_0} = 11.3$ ) was assigned.

As in the previous cases, unless explicitly stated, all of the relevant thermo-physical properties are found in Table 2, with boundary conditions, consisting of zero flux and periodic conditions, as shown in Figure 1. The domain mesh resolution,  $N_x, N_y$ , consisted of 600 x 300 lattice points respectively, with discretization size  $\Delta x = \Delta y = 0.8W_0$ . The domain was initialized with a uniform liquid phase of constant composition ( $\phi = -1, u_0 = -0.3$ ), and included a solid-phase seed of radius  $3\Delta x$ , placed at the lower boundary ( $x = 0, y = N_y/2$ ). As stated, the temperature was allowed to vary according to Equation 19 and simulations involving two different thermal gradients were considered, namely:  $G = 80,000 \text{ K/m}$  and  $G = 120,000 \text{ K/m}$ . A pulling velocity of  $100 \mu\text{m/s}$  was maintained in each case. The simulations ran for approximately  $4.14\text{E}5$  time steps ( $\sim 2.07 \text{ s}$  with  $\Delta t = 5.0e - 6 \text{ s.}$ ) with a corresponding pulling distance ( $V_p t$ ) of  $2.07 \times 10^{-4} \text{ m}$ . The computational run time for each simulation was approximately 48 hr.

Figure 7 shows the evolution of the phase-field for  $G=80\text{E}3 \text{ K/m}$  and  $G=120\text{E}3 \text{ K/m}$ . As indicated, and consistent with previous results (Badillo and Beckermann 2006; Takaki et al. 2016), the solid seed is observed to evolve in time, forming distinctive secondary dendritic arm structures that develop at intervals along the unstable solid/liquid interface. At earlier times ( $t \leq 1\text{s.}$ ), very little dendritic variation (primary or secondary) was observed, at later times it was found that the secondary dendritic arms become somewhat more pronounced for  $G=120\text{E}3 \text{ K/m}$ .

Figure 7. Evolutionary contours of the phase-field ( $\phi$ ) for Al-2wt.%Si comparing the resulting microstructure for two different temperature gradients ( $V_p = 100.0 \mu\text{m/s}$ ).



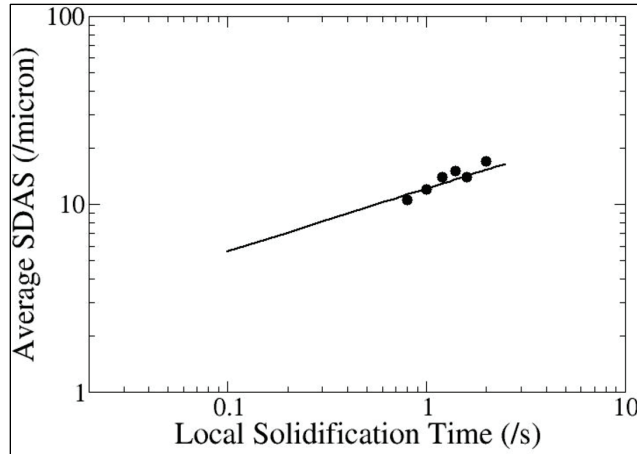
With the secondary arm profiles of Figure 7 (specifically those for  $G=120\text{E}3 \text{ K/m}$ , and  $t > 1\text{s}$ ), corresponding measurements of average arm spacing (SDAS) became tractable. In this work, SDAS measurements were computed between corresponding SDA tip positions and averaged. These measurements were then compared with the theoretical coarsening prediction models of Kattamis (Kattamis and Flemmings 1965), which assume that the SDAS is proportional to the cube root of the solidification time ( $t_f$ ):

$$SDAS = 5.5A(t_f)^{1/3} \quad (29)$$

$$A = -\frac{\Gamma D_L \ln\left(\frac{c_L^f}{c_0}\right)}{m(1-k)(c_L^f - c_0)} \quad (30)$$

Here,  $\Gamma$  is the Gibbs-Thomson coefficient with magnitude shown in Table 1. As shown in Figure 8, good agreement for SDAS between the simulations and the theoretical model were observed.

Figure 8. SDAS as a function of solidification time, showing the cube root dependency and agreement with theoretical values (Kattamis and Flemmings 1965).



## 5 Summary and Conclusions

In this report, the use of the phase-field method for simulating microstructure solidification of metallic alloys was explored. Specifically, the utility of the KKS phase-field method (Kim et al. 1998, 1999) was examined with respect to a series of increasingly complex solidification problems, ranging from one dimensional, isothermal solidification of pure metals to two-dimensional, directional solidification of non-isothermal, binary alloys. Several parametric studies involving variations in thermal gradient, pulling velocity, and anisotropy were also considered and used to assess the conditions for which dendritic and/or columnar microstructures may be generated.

The following conclusions were drawn from this work.

1. The phase-field method used in this study can be used to successfully simulate microstructure evolution of dilute binary alloys corresponding to isothermal, as well as directional solidification.
2. One-dimensional simulations showed a decrease in the maximum concentration for larger interface velocities that resulted from the effects of solute trapping.
3. Simulations of two-dimensional, isothermal solidification revealed the presence of parabolic, dendrite tips evolving along directions of maximum interface energy. Secondary, as well as tertiary dendritic structure was observed and markedly pronounced with the addition of interfacial anisotropy and noise.
4. Consistent with previous results, the two-dimensional simulations of directional solidification resulted in the formation of distinctive secondary dendritic arm structures that evolve at intervals along the unstable solid/liquid interface.
5. Average SDAS measurements from 2-D directional solidification simulations of Al-2wt.%Si showed good agreement with the theoretical model.

In future studies, the solidification of alloys subject to multi-phase/multi-component field phenomenon may be examined, including applications to eutectic alloys and porosity effects. Additionally, implications due to non-equilibrium material properties may be explored.

## References

- Arcella, F. G., and F. H. Froes. 2000. "Producing titanium aerospace components from powder using laser forming." *JOM*, 52(5).
- Badillo, A., and C. Beckermann. 2006. "Phase-field simulation of the columnar-to-equiaxed transition in alloy solidification." *Acta Materialia*, 54.
- Brandl, E., U. Heckenberger, and V. Holzinger. 2012. "Additive manufactured AlSi10Mg samples using Selective Laser Melting (SLM): Microstructure, high cycle fatigue, and fracture behavior." *Materials & Design*, 34.
- Brener, E., and D. Temkin. 1995. "Noise-Induced Sidebranching in the Three-Dimensional Nonaxisymmetric Dendritic Growth." *Phys. Rev. E*, 51(1).
- Caginalp, G., and W. Xie. 1993. "Phase-field and Sharp Interface Alloy Models." *Physical Review E* 48.
- Chao, Y., L. Qi, and H. Zuo. 2013. "Remelting and bonding of deposited aluminum alloy droplets under different droplet and substrate temperatures in metal droplet deposition manufacture." *International Journal of Machine Tools & Manufacture*, 69(3).
- Conti, M. 1997. "Solidification of binary alloys: Thermal effects studied with the phase-field model." *Physical Review E* 55(1).
- Echebarria, B., R. Folch, A. Karma, and M. Plapp. 2004. "Quantitative phase-field model of alloy solidification." *Phys. Rev. E* 70.
- Euler, H. 1768. *Institutiones calculi integralis. Volumen Primum, Opera Omnia, Vol. XI B G Teubneri Lipsiae et Berolini MCMXIII.*
- Fallah, V., S. F. Corbin, and A. Khajepour. 2010. "Process optimization of Ti–Nb alloy coatings on a Ti-6Al-4V plate using a fiber laser and blended elemental powders." *Journal of Materials Processing Technology* 210(4).
- Ferreira, A. F., I. L. Ferreira, J. Pereira da Cunha, and I. M. Salvino. 2015. "Simulation of the microstructural evolution of pure material and alloys in an undercooled melts via phase-field method and adaptive computational domain." *Materials Research* 18(3).
- Ghosh, S., L. Ma, N. Ofori-Opoku, and J. E. Guyer. 2017. "On the primary spacing and microsegregation of cellular dendrites in laser deposited Ni-Nb alloys." *Modelling and Simulation in Materials Science and Engineering* 25(6).
- Gong, S., H. Suo, and X. Li. 2013. "Development and Application of Metal Additive Manufacturing Technology." *Aeronautical Manufacturing Technology* 13(66).
- Heinl, P., A. Rottmair, and C. Korner. 2007. "Cellular titanium by selective electron beam melting." *Advanced Engineering Materials* 9(5).

- Hohenberg, P. C., and A. P. Krekhov. 2015. "An Introduction to the Ginzburg-Landau Theory of Phase Transitions and Nonequilibrium Patterns." *Physics Reports* 572.
- Hu, S., M. Baskes, M. Stan, J. Mitchell. 2007. "Phase-field modeling of coring structure evolution in PuGa alloys." *Acta Materialia* 55(11).
- Kattamis, T. Z., and M. C. Flemmings. 1965. "Dendrite Morphology, Microsegregation and Homogenization of 4340 Low Alloy Steel." *Transactions TMS-AIME* 233.
- Kim, S. G., W. T. Kim, J. S. Lee, M. Ode, and T. Suzuki. 1999. "Large scale simulation of dendritic growth in pure undercooled melt by phase-field model." *ISIJ International* 39(4).
- Kim, S. G., W. T. Kim, and T. Suzuki. 1998. "Interfacial compositions of solid and liquid in a phase-field model with finite interface thickness for isothermal solidification in binary alloys." *Physical Review E* 58(3).
- Kim, S. G., W. T. Kim, and T. Suzuki. 1999. "Phase-field model for binary alloys." *Physical Review E* 60(6).
- Kobayashi, R. 1993. "Modeling and Numerical Simulations of Dendritic Crystal Growth." *Physica D* 63.
- Loginova, I., G. Amberg, and J. Agern. 2001. "Phase-field simulation of non-isothermal binary alloy solidification." *Acta Materialia* 49.
- Maxwell, I., and A. Hellawell. 1975. "A simple model for grain refinement during solidification." *Acta Metallurgica* 23.
- Mullins, W. W., and R. F. Sekerka. 1964. "Stability of a Planar Interface During Solidification of a Dilute Binary Alloy." *J Appl Phys* 35(2)
- Mullis, A. M. 2006. "Quantification of Mesh Induced Anisotropy Effects in the Phase-Field Method." *Computational Materials Science* 36.
- Murray, J. L., and A. J. McAllister. 1984. "The Al-Si (Aluminum-Silicon) System." *Bulletin of Alloy Phase Diagrams* 5.
- Ode, M., S. G. Kim, W. T. Kim, and T. Suzuki. 2001. "Numerical prediction of the secondary dendrite arm spacing using a phase-field model." *ISIJ International* 41(4).
- Ohno, M., and K. Matsuura. 2009. "Quantitative phase-field modeling for dilute alloy solidification involving diffusion in the solid." *Phys. Rev. E*. 79.
- Saito, Y., G. Goldbeck-Wood, and H. Muller-Krumbhaar 1988. "Numerical simulation of dendritic growth." *Physical Review A* 38(4).
- Sakane, S., T. Takaki, M. Ohno, T. Shimokawabe, and T. Aoki. 2015. "GPU-accelerated 3D phase-field simulations of dendrite competitive growth during directional solidification of binary alloy." *IOP Conv. Ser. Mater. Sci. Eng.* 84.
- Spittle, J. A., and S. G. R. Brown. 1989. "Computer simulation of the effects of alloy variables on the grain structures of castings." *Acta Metallurgica* 37(7).

- Takaki, T., S. Sakane, M. Ohno, Y. Shibuta, T. Shimokawabe, and T. Aoki. 2016. "Primary arm array during directional solidification of a single-crystal binary alloy: Large-scale phase-field study." *Acta Materialia* 118.
- Wheeler, A. A., W. J. Boettinger, and G. B. McFadden. 1992. "Phase-field model for isothermal phase transition in binary alloy." *Physical Review E* 45(10).
- Wheeler, A. A., W. J. Boettinger, and G. B. McFadden. 1993. "Phase field model of trapping during solidification." *Physical Review E* 47(4).
- Wilkes, J., Y. C. Hagedorn, and W. Meiners. 2013. "Additive manufacturing of ZrO<sub>2</sub>-Al<sub>2</sub>O<sub>3</sub> ceramic components by selective laser melting." *Rapid Prototyping* 19(1).
- Wolfram, S. 1984. "Cellular automata as models of complexity." *Nature* 311.
- Yan, Y., H. Qi, and F. Lin. 2007. "Three-dimensional Metal Parts by Electron Beam Selective Melting." *Chinese Journal of Mechanical Engineering* 43(6).

## Acronyms and Abbreviations

EBM	Electron Beam Melting
KKS	Kim, Kim and Suzuki
LC	Laser Cladding
PFM	Phase Field Model
SDAS	Secondary Arm Spacing
SLM	Selective Laser Melting
WBM	Wheeler Boettinger and McFadden

# REPORT DOCUMENTATION PAGE

*Form Approved*  
*OMB No. 0704-0188*

Public reporting burden for this collection of information is estimated to average 1 hour per response, including the time for reviewing instructions, searching existing data sources, gathering and maintaining the data needed, and completing and reviewing this collection of information. Send comments regarding this burden estimate or any other aspect of this collection of information, including suggestions for reducing this burden to Department of Defense, Washington Headquarters Services, Directorate for Information Operations and Reports (0704-0188), 1215 Jefferson Davis Highway, Suite 1204, Arlington, VA 22202-4302. Respondents should be aware that notwithstanding any other provision of law, no person shall be subject to any penalty for failing to comply with a collection of information if it does not display a currently valid OMB control number. **PLEASE DO NOT RETURN YOUR FORM TO THE ABOVE ADDRESS.**

<b>1. REPORT DATE (DD-MM-YYYY)</b> May 2020	<b>2. REPORT TYPE</b> Final	<b>3. DATES COVERED (From - To)</b>
--	--------------------------------	-------------------------------------

<b>4. TITLE AND SUBTITLE</b>  Phase-Field Simulations of Solidification in Support of Additive Manufacturing Processes	<b>5a. CONTRACT NUMBER</b>
	<b>5b. GRANT NUMBER</b>
	<b>5c. PROGRAM ELEMENT NUMBER</b> 0603734A

<b>6. AUTHOR(S)</b>  Jeffrey B. Allen, Robert D. Moser, Zachary B. McClelland, Jacob A. Kallivayalil, and Arjun Tekalur	<b>5d. PROJECT NUMBER</b> 479378.2
	<b>5e. TASK NUMBER</b> A1260
	<b>5f. WORK UNIT NUMBER</b>

<b>7. PERFORMING ORGANIZATION NAME(S) AND ADDRESS(ES)</b>  Information Technology Laboratory U.S. Army Engineer Research and Development Center 3909 Halls Ferry Road, Vicksburg, MS 39180-6199  Geotechnical and Structures Laboratory U.S. Army Engineer Research and Development Center 3909 Halls Ferry Road, Vicksburg, MS 39180-6199  Eaton Corportation, Plc. 26201 Northwestern Highway Southfield, MI 48076	<b>8. PERFORMING ORGANIZATION REPORT NUMBER</b>  ERDC TR-20-6
--	---

<b>9. SPONSORING / MONITORING AGENCY NAME(S) AND ADDRESS(ES)</b> U.S. Army Corps of Engineers Washington, DC 20314-1000	<b>10. SPONSOR/MONITOR'S ACRONYM(S)</b>
	<b>11. SPONSOR/MONITOR'S REPORT NUMBER(S)</b>

**12. DISTRIBUTION / AVAILABILITY STATEMENT**  
Approved for public release; distribution is unlimited.

**13. SUPPLEMENTARY NOTES**

**14. ABSTRACT**  
  
For purposes relating to force protection through advancements in multiscale materials modeling, this report explores the use of the phase-field method for simulating microstructure solidification of metallic alloys. Specifically, its utility was examined with respect to a series of increasingly complex solidification problems, ranging from one dimensional, isothermal solidification of pure metals to two-dimensional, directional solidification of non-isothermal, binary alloys. Parametric studies involving variations in thermal gradient, pulling velocity, and anisotropy were also considered, and used to assess the conditions for which dendritic and/or columnar microstructures may be generated. In preparation, a systematic derivation of the relevant governing equations is provided along with the prescribed method of solution.

<b>15. SUBJECT TERMS</b> Materials – Technological innovations Manufacturing processes	Alloys – Microstructure Solidification Materials – Mathematical models	Materials – Mathematical modeling
--	--	-----------------------------------

<b>16. SECURITY CLASSIFICATION OF:</b>			<b>17. LIMITATION OF ABSTRACT</b>	<b>18. NUMBER OF PAGES</b>	<b>19a. NAME OF RESPONSIBLE PERSON</b>
<b>a. REPORT</b> Unclassified	<b>b. ABSTRACT</b> Unclassified	<b>c. THIS PAGE</b> Unclassified			<b>19b. TELEPHONE NUMBER (include area code)</b>